Chapter 6

6.1 Introduction

In this chapter a solid solution of BSFO and BZT has been prepared. The solid solution of $BiFeO_3$ with $BaTiO_3$ system (near the morphotropic phase boundary) have attracted extensive attention due to enhanced piezoelectric response, along with high Tc and lower leakage current behaviour. ZrO_2 acted as an efficient dopant for BT ceramics to obtain high dielectric constant, low dielectric loss, low leakage current, and broad tunability [Sangwan 2018]. The BZT have very high dielectric properties as compared to $BaTiO_3$ due to the pinching effect. The substitution of Zr^{+4} in the Ti^{+4} provides better chemical stability with the ease of lattice expansion to the system. Furthermore, the addition of Zr^{+4} also suppress the possible conversion of Ti^{+4} to Ti^{+3}, which may allow the conduction through hopping of electron. So, the BSFO-BZT system expected to overcome the problems associated with pure $BiFeO_3$ such as extended dielectric losses, leakage current and bismuth volatization.

This study includes the lead-free solid solution of ceramic samples (1-x) $Bi_{0.9}Sm_{0.1}FeO_3$ − (x) $BaZr_{0.15}Ti_{0.85}O_3$ (BSFO − BZT) (x =0.0, 0.1, 0.15, 0.2, 0.25, 0.5) were prepared using mechnochemical solid state reaction method. We have replaced 15% Ti with Zr. BZT with Zr content less than 27% shows normal ferroelectric behavior as its MPB lying below 27% [Rout 2006]. The structural, morphological and temperature dependent dielectric properties, as well as leakage current were investigated. The degree of structural distortion in the BSFO−BZT based perovskite system is explained with theoretical calculation of tolerance factor by using equation 1.1 and graphical representation is shown in fig.6.1.

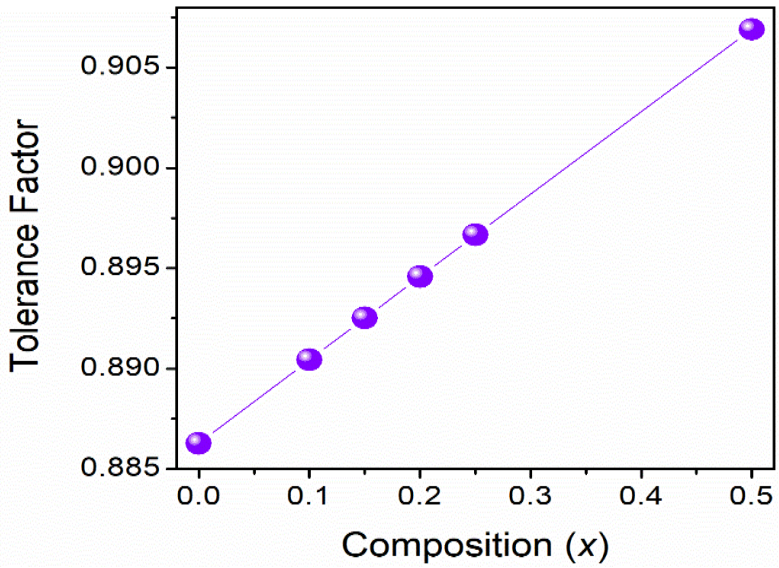

Fig. 6.1: Tolerance factor of {(1-x) $(Bi_{0.9}Sm_{0.1})FeO_3$ − (x) $Ba(Zr_{0.15}Ti_{0.85})O_3$} (BSFO − BZT) (x = 0.0, 0.1, 0.15, 0.2, 0.25, 0.5) solid solution samples.

6.2 Results and discussions

6.2.1 X-ray diffraction

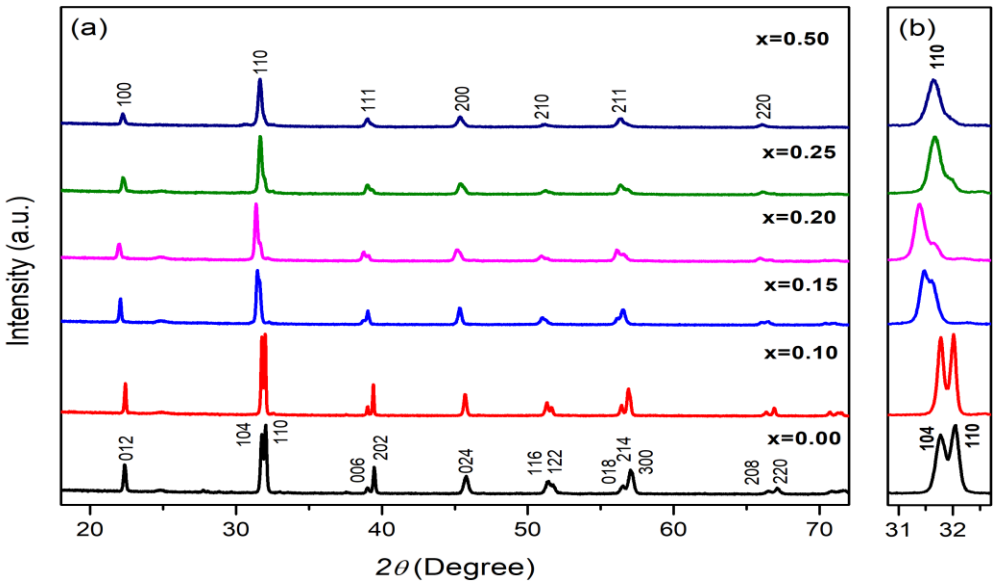

Fig. 6.2: X-ray Diffraction patterns of {(1-x) $(Bi_{0.9}Sm_{0.1})FeO_3$ − (x) $Ba(Zr_{0.15}Ti_{0.85})O_3$} (BSFO − BZT) (x = 0.0, 0.1, 0.15, 0.2, 0.25, 0.5) samples.

Fig. 6.2 shows the room temperature X-ray diffraction graphs of (1-x)BSFO−(x)BZT (x = 0.0, 0.1, 0.15, 0.2, 0.25, 0.5) ceramics. The high intensity diffraction peaks show the formation of the solid solution of BSFO-BZT. All the diffraction peaks were indexed by using software X'pert high score. It is noticed that for the composition $x \leq 0.025$, *R3c* phase was confirmed and indexed with the standard JCPDS file (#86-1518) [Jha *et al.* 2014]. In the pure BSFO samples a minimal amount of impurity of $Bi_2Fe_4O_9$ was identified. The impurity phases get effectively suppressed with the doping of BZT. The split peaks at ~32° (110, 104) and ~37° (006, 202) show that the BSFO-BZT samples exhibit rhombohedral symmetry. For x = 0.5, the structure becomes pseudocubic and matched with a tetragonal crystal system [Cai 2014]. Also, the peaks (110,104) merged to 110 and (006, 202) merged and converted to 111, which also confirms the existence of tetragonal phase to the samples having higher BZT content. Further, it is noticed that the peaks get shifted towards the lower angle side on increasing BZT content in BSFO. This shifting of diffraction peaks is due to the increasing lattice parameters because in the BSFO-BZT system, ionic radius of Ba^{2+} (135 pm) is bigger than Bi^{3+} (110 pm), ionic radii of {Zr^{4+} (80 pm), and Ti^{4+} (65 pm)} are greater than that of Fe^{3+} (64 pm) [Jha *et al.* 2014]. For the confirmation of structural changes in the BFO-BZT system, the X-ray graphs were refined with Rietveld's refinement using FULL PROF refinement software shown in Fig. 6.3.

The peak shapes of the entire sample were explained with Pseudo-Voigt function. The samples of (1-x) BSFO - (x)BZT up to $x \leq 0.025$ were fitted with *R3c* space group and a good agreement set between experimental and refined data. For x = 0.5, the crystal system changes to tetragonal so, fitted with *P4mm* space group. Fig 6.4 shows the unit cell volume.

It is observed that the unit cell volume increases with doping in the samples due to increasing lattice parameters and also may be because of suppression of impurity phases.

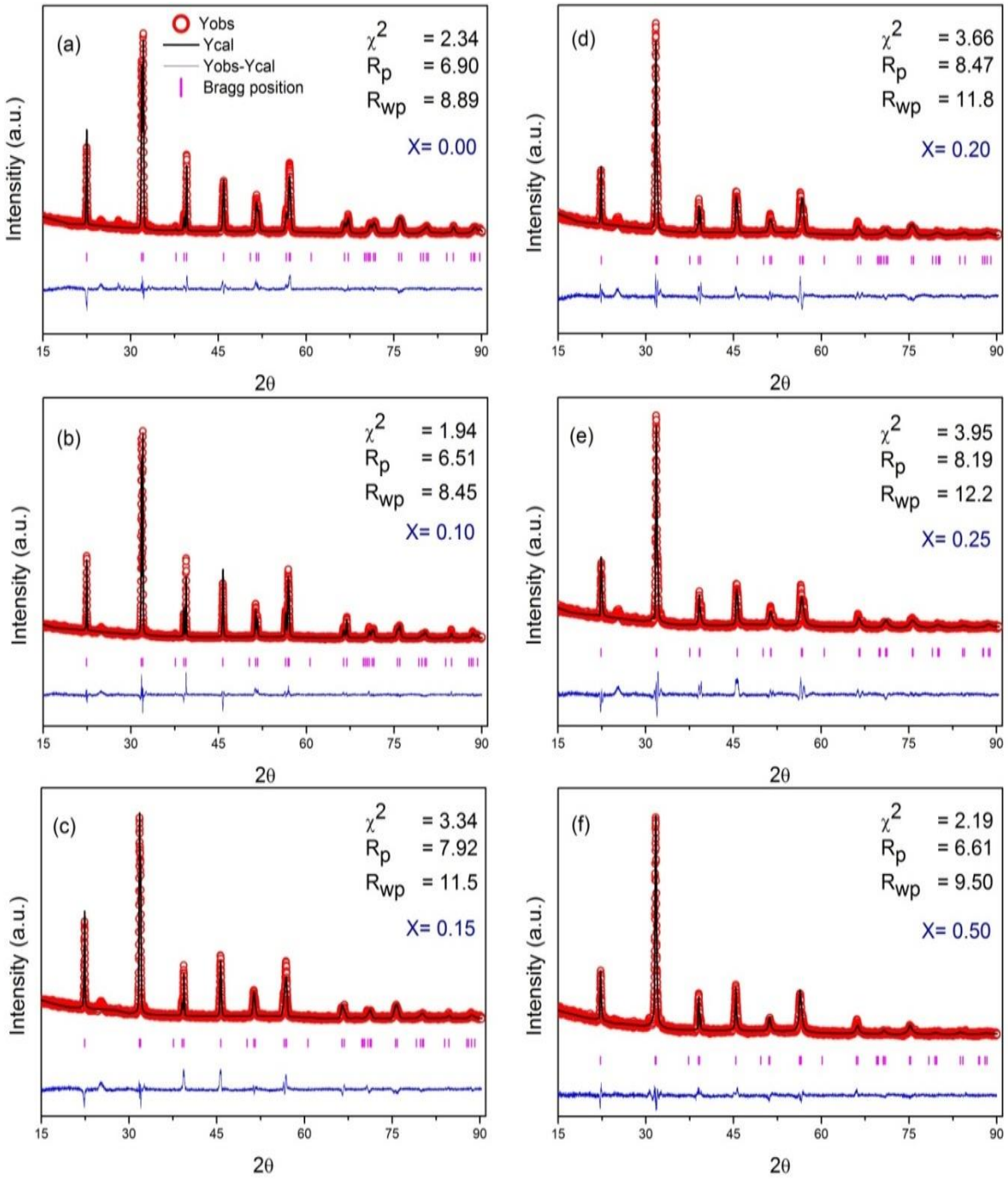

Fig. 6.3: Rietveld analysis of {(1-x) $(Bi_{0.9}Sm_{0.1})FeO_3$ − (x) $Ba(Zr_{0.15}Ti_{0.85})O_3$} (BSFO − BZT) (x = 0.0, 0.1, 0.15, 0.2, 0.25, 0.5) samples.

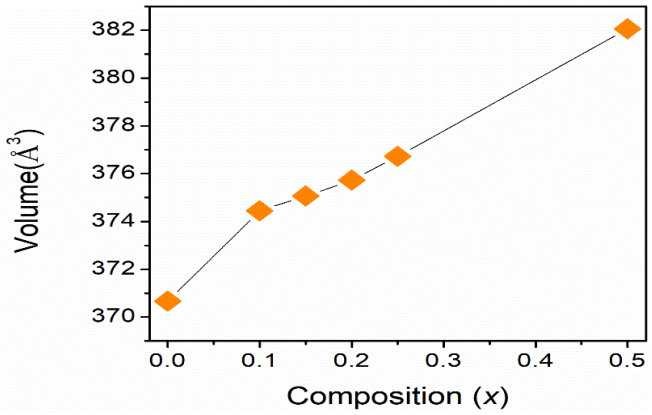

Fig. 6.4: Volume of {(1-x) ($Bi_{0.9}Sm_{0.1}$)FeO_3 − (x) Ba($Zr_{0.15}Ti_{0.85}$)O_3} (BSFO − BZT) (x = 0.0, 0.1, 0.15, 0.2, 0.25, 0.5) solid solution samples.

6.2.2 Scanning electron microscopy

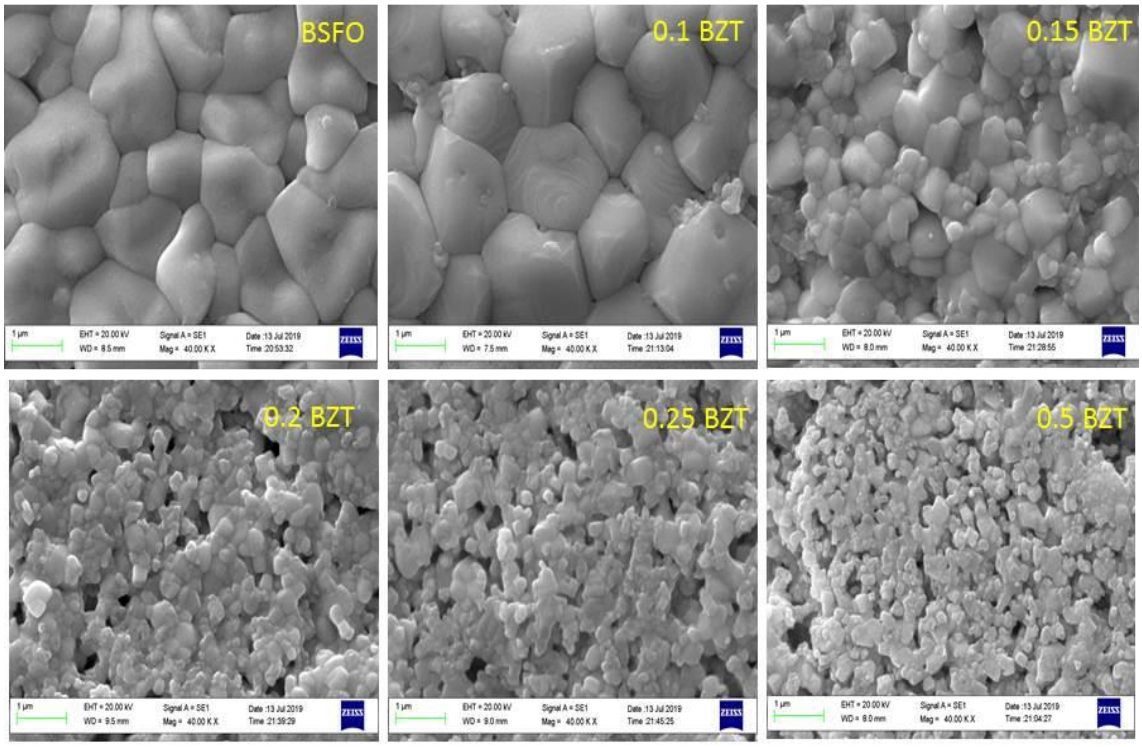

Fig. 6.5: SEM micrographs of {(1-x) ($Bi_{0.9}Sm_{0.1}$)FeO_3 − (x) Ba($Zr_{0.15}Ti_{0.85}$)O_3} (BSFO − BZT) (x = 0.0, 0.1, 0.15, 0.2, 0.25, 0.5) solid solution samples.

Fig. 6.5 shows the SEM micrographs of (1-x) BSFO−(x) BZT (x = 0.0, 0.1, 0.15, 0.2, 0.25, 0.5) ceramics samples. It is observed that the grain sizes reduce with increasing BZT content. The grains start to dilute their distinct shapes and leads to the formation of irregular shaped tiny semispherical grains with broader size distribution, with the addition of BZT to the samples. This kind of geometrical changes can be correlated to the structural changes to the crystal. As in case of BSFO it was found to be of rhombohedral in nature and it transformed to the tetragonal crystal system with BSFO-BZT system at (x=0.5) [Cai *et al.* 2014; Choudhary *et al.* 2007].

In addition, the structure becomes porous with increasing content of BZT and the variation of grain size can be explained on the basis of dissimilar melting point of both components. As the existence of higher melting point component (BZT in this case) provide more nucleation sites, which hinder the grain growth, resulted to lowering the grain size [Cai *et al.* 2009]. To maintain the stoichiometric intact and consideration of Bismuth volatility, sintering temperature could not exceed above 850 °C. So, the grain boundary effects could not be explained in BFO rich samples in case of BFO−BZT system [Choudhary *et al.2007*].

6.2.3 Dielectric and impedance study

Fig. 6.6 (a-c) shows the dielectric behavior of (1-x) BSFO−(x) BZT (x =0.0, 0.1, 0.15, 0.2, 0.25, 0.5) samples were recorded at temperature range between 303K-773K and frequency range between 20Hz to 20MHz. Intending to a better understanding of the dielectric behavior of the above samples ε', ε" and tanδ at 10 kHz frequency are plotted in fig. 6.6. It is revealed that all these samples exhibit an increasing trend for real and imaginary part of permittivity with temperature. This behavior may be explained due to the

enhancement of space charge polarization with rising temperature [Chen *et al.* 2000; Sharma *et al.* 2019]. The increasing dielectric constant may also be attributed to the ease of grain orientation and mobility, which provide easy polarization to the sample at high temperature [Nair *et al.* 2022].

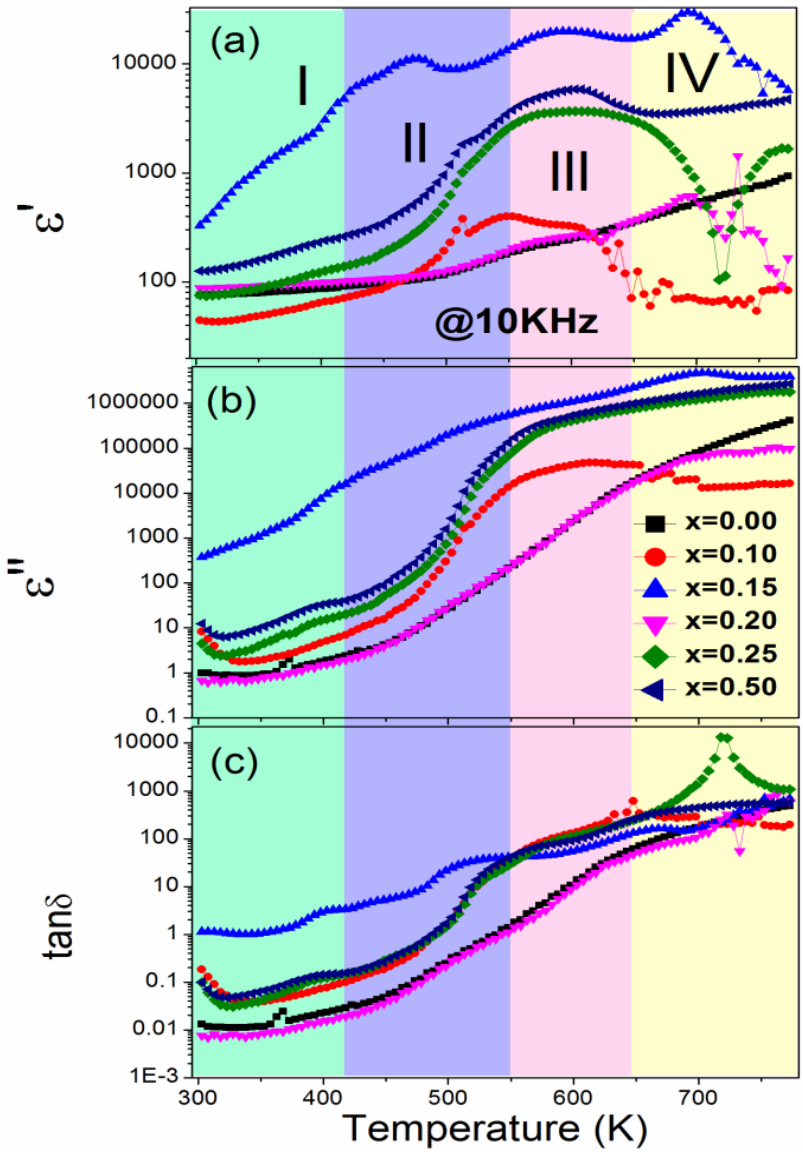

Fig. 6.6: ε', ε'' and tanδ of {(1-x) $(Bi_{0.9}Sm_{0.1})FeO_3$ − (x) $Ba(Zr_{0.15}Ti_{0.85})O_3$} (BSFO − BZT) (x = 0.0, 0.1, 0.15, 0.2, 0.25, 0.5) solid solution samples.

All the samples excepting pure BSFO, shows anomalies in particular temperatures range which are divided into four regions I(350K to 450K), II(450K to 550K), III(550K to 650K), and IV(650K to 750K). The dielectric constant at a particular frequency of 10 kHzfor pure BSFO sample increases with frequency with existence of minor kinks. Initially the addition of BZT resulted in decreasing dielectric constant up to 450 K (starting of region II), and achieve its maximum value of 398 at 548K within region II, afterward it shows a decrement within region III and become constant in region IV. With further addition of BZT at x = 0.15, the dielectric constant increases and found to be maximum among all studied samples, with appearance of three broad shoulders corresponding to 478K, 593K, 693K in region I, II and III respectively. As it achieves highest dielectric constant with well distinguishable anomalies, it may be considered as a morphotropic phase boundary (MPB) for BZT doping within BSFO samples. In case of x = 0.20, it follows nearly similar dielectric profile with several fluctuations at higher temperature having two broader peaks at 693K in region III and 733K in region IV. For x = 0.25, it shows a plateau with a peak at 608K within region III and another hump at around 768K within region IV. For x =0.5, the dielectric constant increases again with two major humps at 513K within region II and 603K within region III.

As shown in Fig. 6.7 the room temperature dielectric properties of got improved with incorporation of BZT in to BSFO for all over the series excepting x=0.1. This enhancement can be justified on the basis of oxygen vacancies suppression and the instabilities within oxidation states of Fe [Sharma *et al.* 2019].

The dielectric anomalies within temperature region I(350 K to 450 K)exists due to transition temperature(Tc) of BZT phase(the hump increased with doping level) or due to small localized polaron hopping within sample[Sharma *et al.* 2019, Jha *et al.2014*].

The anomaly within the region II, may be associated to the bismuth vacancy with triple negative charge (V_{Bi}''') or an oxygen vacancy with double positive charge (V_{Bi}''') or any other charge deficiency [Nair *et al.* 2022]. The dielectric anomalies within region III, can be correlated to the magnetoelectric coupling with magnetic transition (Antiferromagnetic state to paramagnetic state) known as Neel temperature (T_N) for pure BFO sample [Ma *et al.* 2009; Polomska *et al.* 1974; Jia *et al.* 2009; Catalan *et al.* 2009]. In case of region IV, these anomalies are due to the hopping of small sized polaron or movement of ionized oxygen vacancies [Sharma *et al.* 2019].

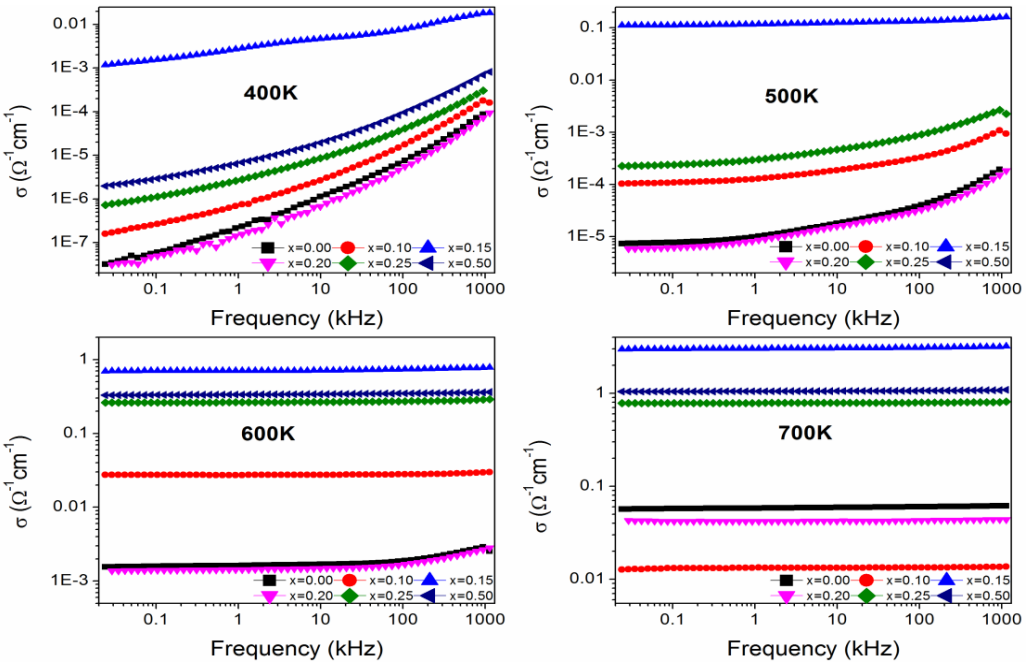

Fig. 6.7: Conductivity plots of {(1-x) ($Bi_{0.9}Sm_{0.1}$)FeO_3 − (x) Ba($Zr_{0.15}Ti_{0.85}$)O_3} (BSFO − BZT) (x = 0.0, 0.1, 0.15, 0.2, 0.25, 0.5) solid solution samples.

The dielectric anomalies along with the response of these ferroelectric samples within applied electric field may be explained on behalf of the conduction mechanism being takes place within it, and its variation with increasing temperature. As the frequency dependent conductivity can be determined using following relation with permittivity (6.1):

$$\sigma_{Ac} = \varepsilon_r \varepsilon_o . (2\pi f) . tan\delta \quad (6.1)$$

Where 2πf represent the angular frequency (ω), ε_r and ε_o are relative and free space permittivity respectively [Nair *et al.* 2022].

Fig. 6.6 shows the variation of ac conductivity (σ_{Ac}) with increasing frequency for all four regions respectively. As it is revealed that the ac conductivity of all doped samples increased within region I, II and III excepting the x = 0.20. The sample having x = 0.10 and x = 0.2 both shows abnormal behavior within region IV, the overall ac conductivity found to be enhanced with doping of BZT within BSFO samples.

In case of multiferroic materials, the frequency dependent ac conductivity may also be used to determine the electron hopping phenomena or polaron mechanism associated with the charge carriers. Generally, Polarons are electrons surrounded with virtual phonons formed during the movement of electrons within the applied electric field. These movements of electrons are responsible to polarize the adjoining lattice and polarons are created within the sample. The size of these polarons can be correlated to the degree of lattice distortion being introduced during the generation of one polaron [Nair *et al.* 2022, Basuray *et al*. 2009].

If the lattice distortion will be less than lattice constant of unit cell, it will generate small polaron while larger distortion will be responsible to generation of larger polaron within sample. The polaron size within these samples can be analyzed with the frequency

dependent ac conductivity, the increasing trend for curve represent the existent of small polarons and larger polarons for the reverse. Hence it is clear that initially, majority of conduction are due to the small polarons for all samples but the size of polaron keep growing with increasing temperature. The straight-line behavior for the ac conductivity represents the mixed impact of large and small polaron within the sample. These entire samples consist of a frequency independent ac conductivity within the IV temperature region.

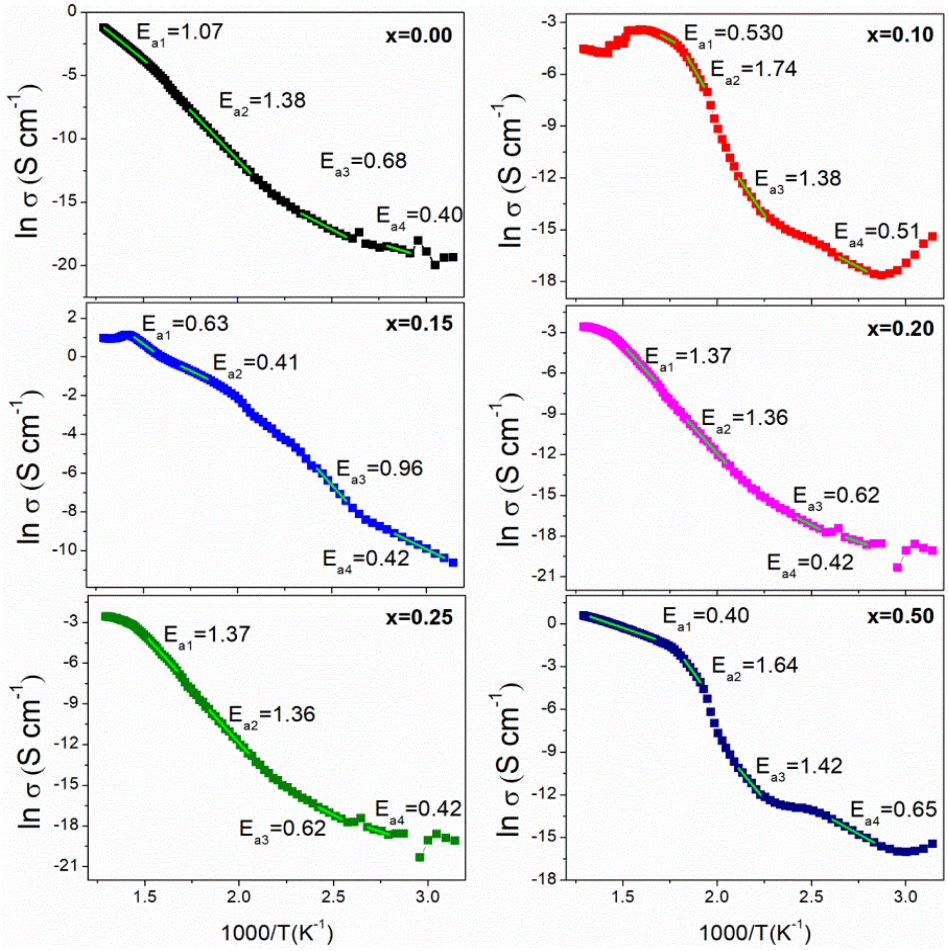

Fig. 6.8: Activation energy calculated from real part of permittivity (ε') of {(1-x) $(Bi_{0.9}Sm_{0.1})FeO_3$ − (x) $Ba(Zr_{0.15}Ti_{0.85})O_3$} (BSFO − BZT) (x =0.0, 0.1, 0.15, 0.2, 0.25, and 0.5) solid solution samples.

The high temperature dielectric behavior shows a direct or indirect dependency with various factors such as electric field intensity, internally generated defects, microstructural orientation, and ionic substitutions. It is widely accepted that dielectric relaxation in ferroelectric materials is very sensitive to electric field, temperature, intrinsic defect, domain configuration, ionic substitution, *etc.*, as they can modify the polarization configuration. It has been reported that the defects such as A-site vacancies, space charge electrons, oxygen vacancies, or other impurities are responsible for the dielectric relaxation in high temperature region [Zhang *et al.* 2014].

To validate the particular conduction mechanism within each temperature region, ln σ_{ac} are plotted with 1000/T and the activation energy (E_a) is estimated with the help of Arrhenius equation:

$$\sigma_{ac} = \sigma_o e^{(-E_a/k_B.T)} \quad (6.2)$$

Where σ_o is the limiting conductivity at elevated temperature (pre-exponential term), E_a is process Activation energy, K_B is Boltzmann constant ($1.38x10^{-23}$ $J.K^{-1}$), T meant for temperature in Kelvin (K) [Orr *et al. 2021*].

The measured activation energies for each temperature region are shown in Fig. 6.8. It was found that the values of combined activation energies for region I(0.40-1.37 eV) and II(0.41-1.74 eV), are dominated over the combined activation energies for region III(0.62-1.42 eV) and IV(0.40-0.65 eV) [Dwivedi *et al.* 2001].The Conduction mechanism within all four regions can be explained with the generation and migration of oxygen vacancies in the fig.8. The generation of oxygen vacancies with varying temperature can be denoted as:

$O_0^{2-} \rightarrow \frac{1}{2}O_2 + V_0$ (Formation of one oxygen vacancy during high temperature sintering process)

$V_0 \rightarrow V_0^{\cdot} + e'$ (Formation of singly ionized oxygen vacancy with releasing of one electron)

$V_0^{\cdot} \rightarrow V_0^{\cdot\cdot} + e'$ (Formation of doubly ionized oxygen vacancy with releasing of one electron)

On the basis of activation energies, it can be understood that the conductivity of these samples within region I is dominated by migration of $V_0^{\cdot\cdot}$(0.5-1.0 eV), Region II is dominated by band conduction (E_a value beyond 1eV), Region III is equally contributed by $V_0^{\cdot\cdot}$ and band conduction, Region IV is dominated by $V_0^{\cdot}$ [Dwivedi *et al.* 2001; Zhang *et al.* 2014]. The activation energy values also suggest that all these samples are able to maintain its mixed stoichiometric significance of $ABO_{2.95}$ and ABO_3 (E_a =1.0 to 2.0 eV) and $ABO_{2.9}$ (corresponding to E_a =0.5) within region IV [Zhang *et al.* 2014].

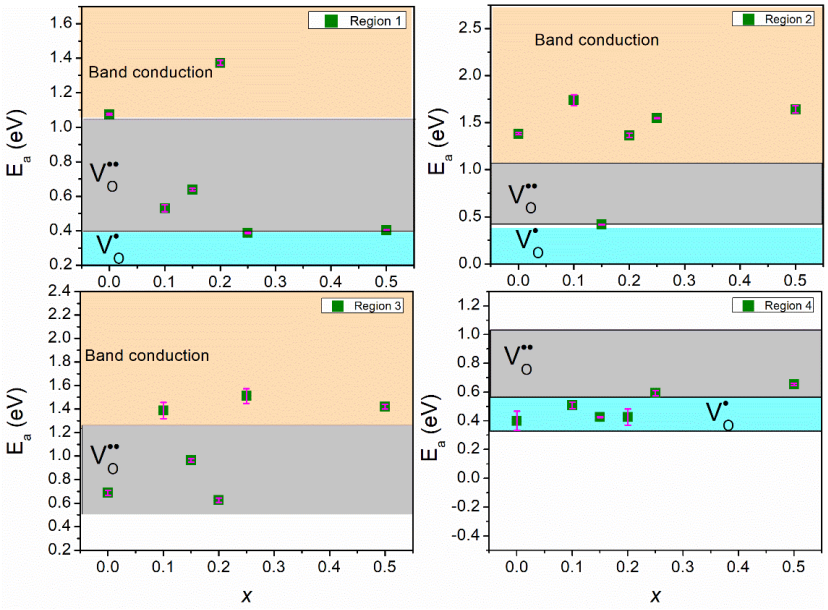

Fig. 6.9: Conduction mechanism of {(1-x) $(Bi_{0.9}Sm_{0.1})FeO_3$ − (x) $Ba(Zr_{0.15}Ti_{0.85})O_3$} (BSFO − BZT) (x = 0.0, 0.1, 0.15, 0.2, 0.25, 0.5) solid solution samples.

To study the dielectric and electrical properties simultaneously or to confirm the presence of various electrical heterogeneities within prepared samples, the real (Z′) and imaginary (Z″) part of impedance are plotted with increasing frequency from 20 Hz to 1 MHz range for each of temperature region separately [Kolte *et al.* 2015, Thansanga *et al.* 2019]. As shown in fig. 6.10 the real part of impedance (Z′) found to be decreased with temperature within low frequency region. It depicts that the all these samples have negative temperature coefficient of resistance (NTCR). The results also depicts that the real part of impedance found to be decreased with increasing frequency in the temperature regions (350K to 450K), it may be explained due the reduction of charge barrier or releasing space charge. Afterward the material starts showing a reverse behavior with increasing temperature and found to be in a reverse trend within temperature region IV. The existence of a hump within temperature region II, found to be at lower frequency region which may be due to the role of grain boundary. The peak existing at higher frequency region within temperature region III may be due to the grain contribution to the real impedance [Kolte *et al.* 2015].

Also, Fig. 6.11 shows the frequency dependent imaginary impedance (Z″) within all four regions. The result shows that it follows the similar diminishing trend with temperature. The results also suggest that as the temperature keep growing; the frequency dependency of imaginary part of impedance (Z″) got minimized. As there is a peak shifting noticed within the temperature region II, which may explain the phenomena associated to the maximum capacitive effect with doping of BZT to the sample [Thansanga *et al.* 2019].

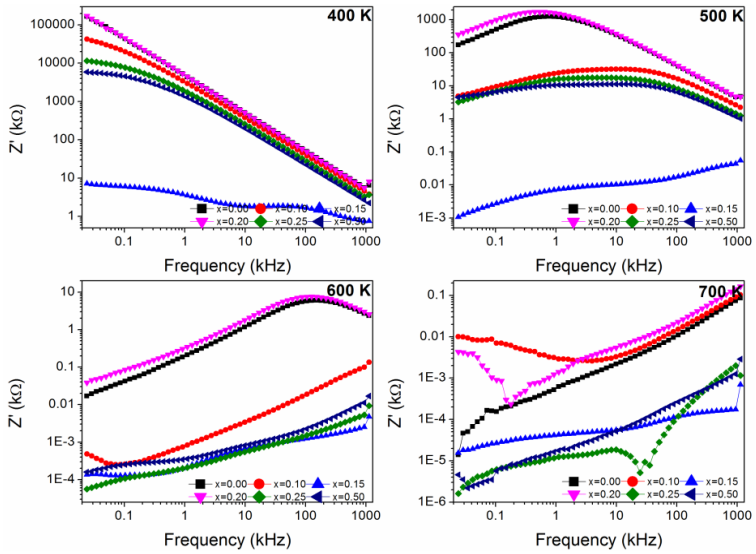

Fig. 6.10: Z′ vs. Frequency plot within different temperature region of {(1-x) $(Bi_{0.9}Sm_{0.1})FeO_3 - (x)\ Ba(Zr_{0.15}Ti_{0.85})O_3$} (BSFO − BZT) (x = 0.0, 0.1, 0.15, 0.2, 0.25, 0.5) solid solution samples.

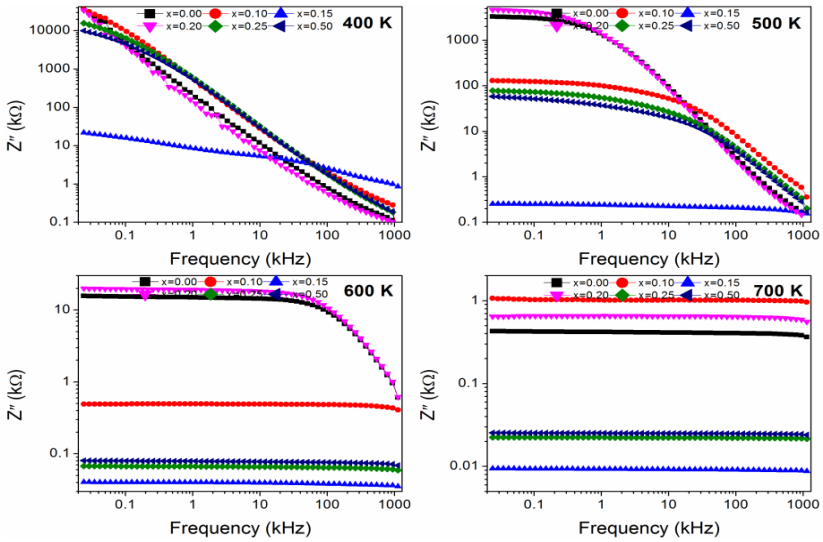

Fig. 6.11: Z″ vs. Frequency plot within different temperature region of {(1-x) $(Bi_{0.9}Sm_{0.1})FeO_3 - (x)\ Ba(Zr_{0.15}Ti_{0.85})O_3$} (BSFO − BZT) (x = 0.0, 0.1, 0.15, 0.2, 0.25, 0.5) solid solution samples.

6.2.4 Leakage current

Fig. 6.12 shows the leaky behavior of all the (1-x) BSFO−(x) BZT (x= 0.0, 0.1, 0.15, 0.2, 0.25, 0.5) ceramic samples recorded at room temperature in order to study the conduction mechanism. All the samples were subjected to the electric field up to 100 V/cm at room temperature and leakage current densities were measured against the varying electric field. It is observed that the leakage current is increases with the applying field for all the samples. The values of current densities for all the samples are ***3.5 × 10^{-2}, 3.5 × 10^{-5}, 1.2 × 10^{-9}, 1.4 × 10^{-10}, 3.8 × 10^{-10}, and 2.6 × 10^{-8}*** **A/cm^2** respectively.

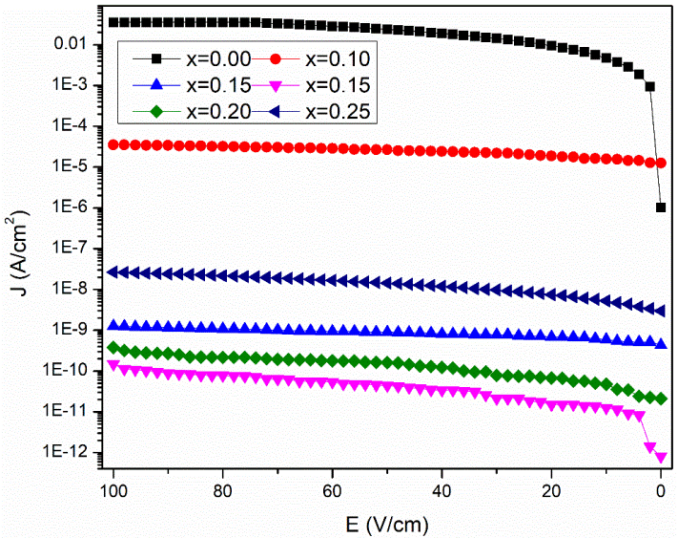

Fig. 6.12: Leakage current of {(1-x) ($Bi_{0.9}Sm_{0.1}$)FeO_3 − (x) $Ba(Zr_{0.15}Ti_{0.85})O_3$} (BSFO − BZT) (x = 0.0, 0.1, 0.15, 0.2, 0.25, 0.5) solid solution samples.

The transport behaviour in $BiFeO_3$ generally depends on three factors: (i) concentration of oxygen vacancies, which provide a path for thermally stimulated charge carriers to flow under applied electric field [Singh *et al.* 2011] (ii) variable oxidation state of Fe ions (Fe^{2+} and Fe^{3+}), which provide hopping of Fe^{2+} ions in the vicinity of electric field

[Sharma *et al.* 2019] (iii) density of materials and volume of grains and grain boundaries [Uniyal *et al.* 2008]. It is noticed that current density reduces with increasing BZT content up to x = 0.20 which may be accredited to a decrease in defects (oxygen vacancies) which improves the ferroelectric properties. For x = 0.25 and x = 0.5 leakage current density increases due to grain density. The mechanism of the leakage current is based on the conduction.

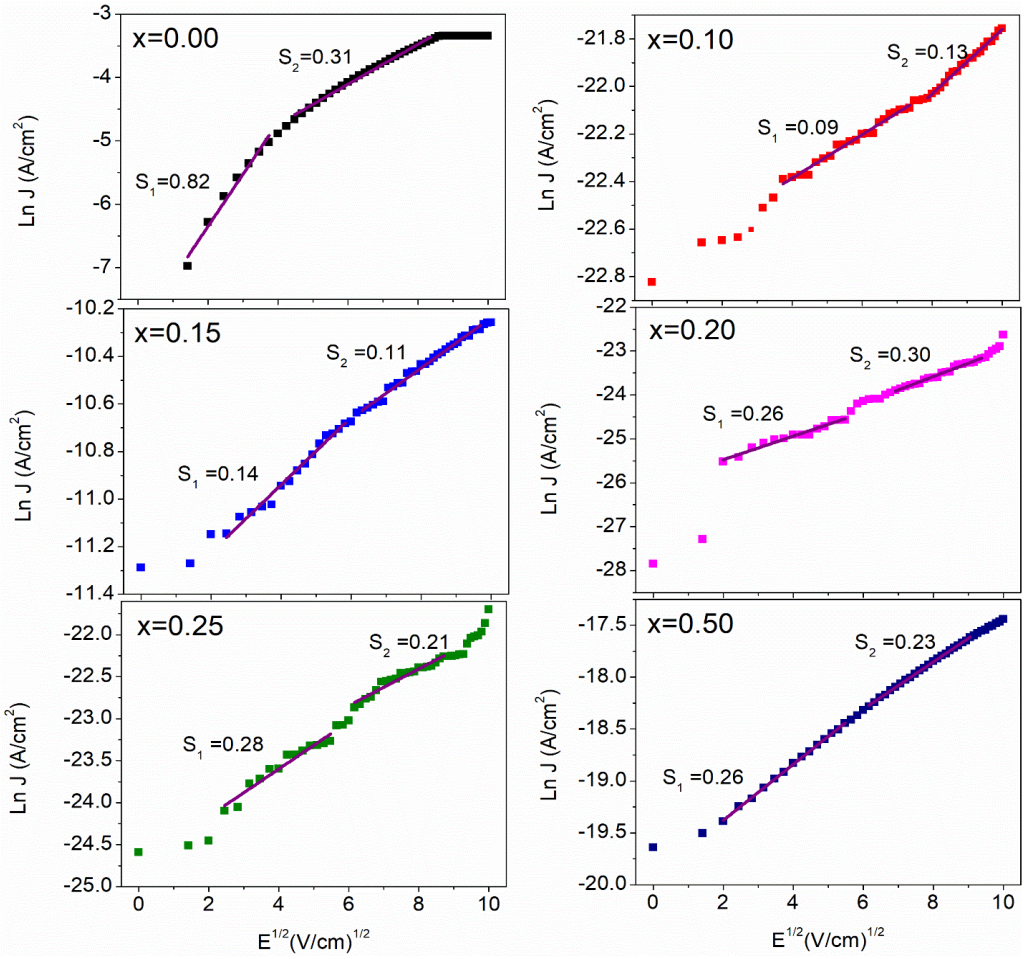

Fig. 6.13: Schottky emission of {(1-x) ($Bi_{0.9}Sm_{0.1}$)FeO_3 − (x) Ba($Zr_{0.15}Ti_{0.85}$)O_3} (BSFO − BZT) (x = 0.0, 0.1, 0.15, 0.2, 0.25, 0.5) solid solution samples.

There are two categories of conduction mechanisms (i) bulk-limited conduction in which space charge-limited conduction (SCLC) and Poole–Frenkel emission (PF) exists; (ii) interface-limited conduction mechanisms in which Schottky emission (SE) and Fowler-Nordhiem tunneling (FN) exists [Uniyal *et al.* 2008]. These models could provide better understanding of the leakage current density of the samples. Therefore, the SCLC and Schottky emission (SE) models were studied in detail to obtain further insight into the electrical properties [Sharma *et al.* 2019].

SE arises from a difference in Fermi levels between a metal electrode and an insulator. The energy difference creates a potential barrier between the metal and insulator that charges must overcome. The current density across a Schottky barrier is given by equation 6.3.

$$J = R_c \mathrm{T}^2 \, exp - \left[\frac{\varphi_b}{kT} - \frac{q}{kT} \left(\frac{q I_e}{4\pi\varepsilon_0 \varepsilon_\omega} \right)^{1/2} \right] \qquad (6.3)$$

Where, J is current density, R_c is Richardson constant, I_e is trap ionisation energy, φ_b is voltage barrier, E is the electric field of the dielectric, T is absolute temperature, k is the Boltzmann constant, ε_0 is permittivity of free space, and ε_ω is the optical dielectric constant [Makhdoom *et al.* 2012]. Fig 6.13 shows the SE conduction mechanism with ln J vs. $E^{½}$ plots of all the samples. In order to confirm the leakage current behavior governs by Schottky emission, the K value coinciding with the intrinsic material properties should be considered. ε_ω can be derived from linear fitting of the curves. The refractive index (n) of BFO is 2.5 here, $\varepsilon_\omega = n^2$ thus, ideal optical dielectric permittivity of pure BFO is 6.25. It is observed from the plots that there is more deviation of dielectric constant than the pure BFO. So, SE emission is ruled out [Sharma *et al.* 2019, Makhdoom *et al.* 2012].

In order to determine the leakage current behaviour in the low power regions of samples space charge limited conduction (SCLC) was studied. Fig. 6.14 shows the log J vs. log E curves indicating the SCLC mechanism for all the samples explained on the basis of Lampert's theory equation:

$$J \propto E^{\alpha}$$

Where, α is slope of curves. The value of α<1 indicates grain boundary limited conduction; α = 1 for ohmic conduction; and α≤2 for space charge limited conduction.

It is noticed that in pure sample ohmic conduction is dominating while in BZT doped samples grain boundary limited conduction is dominating which is indicating that oxygen vacancies and impurity phases are decreases [Sharma *et al.* 2019].

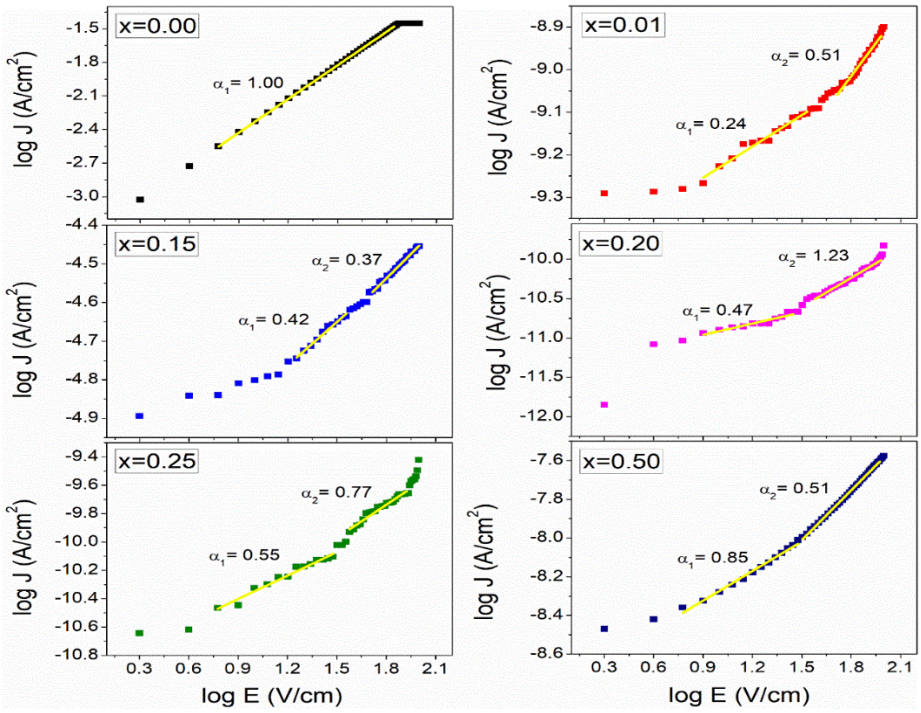

Fig. 6.14: Space charge limited conduction of {(1-x) $(Bi_{0.9}Sm_{0.1})FeO_3$ − (x) $Ba(Zr_{0.15}Ti_{0.85})O_3$} (BSFO − BZT) (x = 0.0, 0.1, 0.15, 0.2, 0.25, 0.5) solid solution samples.

6.3 Summary

Multiferroic-perovskite based Solid solution of ceramic samples having a general formula of (1-x) $Bi_{0.9}Sm_{0.1}FeO_3$ − (x) $BaZr_{0.15}Ti_{0.85}O_3$ (BSFO−BZT) (x = 0.0, 0.1, 0.15, 0.2, 0.25, 0.5) were successfully prepared by conventional solid-state route. The structural analysis confirms that BSFO retains its rhombohedral symmetry (*R3c* space group) up to the x = 0.025, further addition of BZT changes the crystal symmetry to tetragonal with *P4mm* space group. The SEM micrographs showed that the increasing BZT content leads to the reducing grain sizes along with diluted irregular shaped grains. The sample x=0.15, shows maximum dielectric values among all prepared BSFO-BZT samples, may be considered as the MPB limit for the proposed system. The activation energy values suggest the presence of mixed stoichiometric significance of $ABO_{2.95}$ and ABO_3 below 650 K temperature and $ABO_{2.9}$ afterward. The temperature and frequency dependent impedance analysis confirm the existence of NTCR (reverse trend with resistance and temperature) for all samples. The sample x =0.20 shows the least possible leakage current value within the series. As a result, the sample x =0.15 satisfies both the parameters, it achieved largest dielectric constant along with a moderate leakage current density value (**$1.2 \times 10^{-9} A/cm^2$**) which is quite lower than pure BSFO. Finally, the obtained results suggest the feasibility for large scale productivity of BSFO-BZT solid solutions having better dielectric properties with minimized leakage current density to fabricate multiferroic devices.